Engineering Fracture Mechanics 326 (2025) 111431

Contents lists available at ScienceDirect

Engineering Fracture Mechanics

journal homepage: www.elsevier.com/locate/engfracmech

Integrated experimental and multi-trapping finite element approach to estimate critical hydrogen concentrations and embrittlement in CrMo steel☆

Chiara Colombo [a,*], Luis Borja Peral [b], Marcos Bueno [b], Inés Fernández-Pariente [b]

[a] Politecnico di Milano, Department of Mechanical Engineering, Via La Masa 1, 20156 Milano, Italy
[b] University of Oviedo, Campus of Gijón, East building, 33203 Gijón, Spain

ARTICLE INFO

Keywords:
Hydrogen embrittlement
Hydrogen trapping
Cohesive zone modelling
Fracture toughness
CrMo steel

ABSTRACT

The paper presents a numerical study on a CrMo martensitic steel experiencing hydrogen embrittlement with enhanced localized plasticity mediated by decohesive mechanisms. Experimental inputs, including stress–strain curves, trap energies and densities, initial hydrogen concentration C_{L0} and diffusion coefficient, were inputted into a cohesive zone model. The model suggests quantifying embrittlement with three parameters: the critical concentration at the tip, the concentration peak ahead of the tip and the distance of the peak from the tip. The simulations at the two test speeds of 1 and 0.01 mm/min revealed that dislocation traps dominate at the crack initiation, with a critical hydrogen concentration at the tip of 2.5 C_{L0}, independent of the test speed. As propagation advances, the critical hydrogen concentration decreases to the asymptotic value of 1.5 C_{L0}. This trend changes as a function of the test speed: the lower the speed, the higher the time hydrogen has to move to the tip, the higher the concentration peak and its distance from the tip, and the higher the embrittling effect. These numerical results help to describe and quantify the experimental observations, e.g. embrittlement index and fracture surfaces. Overall, the approach highlights the capability and utility of numerical models in understanding hydrogen diffusion and embrittlement, offering insights for designing metallic materials sensitive to testing conditions.

1. Introduction

Hydrogen is increasingly recognized as a promising energy carrier and plays a pivotal role in advancing the green transition and achieving sustainable goals, as mentioned in a recent report by the European Commission [1]. However, optimizing its production, particularly through electrolysis powered by renewable energy, i.e. green hydrogen, presents significant challenges. It is essential to build a reliable and performing infrastructure including pipelines and storage facilities. To this end, designers must overcome significant technical difficulties, particularly when high pressures are involved.

CrMo steels, commonly employed to design pressure vessels in the petrochemical industry, are good candidates to contain hydrogen gas up to the most demanding pressures, e.g. 700 bars. However, both research and industry require reproducible

☆ This article is part of a special issue entitled: 'Hydrogen Embrittlement' published in Engineering Fracture Mechanics.

* Corresponding author.
E-mail address: chiara.colombo@polimi.it (C. Colombo).

https://doi.org/10.1016/j.engfracmech.2025.111431
Received 5 February 2025; Received in revised form 12 July 2025; Accepted 18 July 2025
Available online 20 July 2025

Nomenclature

a	Crack length
$\overline{a}$	Lattice parameter
A	Elongation
A_r	Molar mass of iron
b	Burgers vector
c	Interface carbide-matrix
C_{app}	Apparent concentration
C_{irrev}	Concentration in irreversible traps
C_L	Concentration in the lattice
$C_{L,0}$	Initial concentration in the lattice
C_{peak}	Hydrogen peak concentration ahead the crack tip
C_{rev}	Concentration in reversible traps
C_T	Concentration in the traps
C_{tip}	Hydrogen concentration at the crack tip
d	Carbide size
d_{peak}	Distance from the crack tip and the peak of concentration
D	Damage
D_{app}	Apparent diffusion coefficient
D_g	Grain size
D_L	Diffusivity in the lattice
E_a	Activation energy
E_b	Binding energy
EI	Embrittlement index
E_L	Activation energy in the lattice
f	Carbide volume fraction
J_{max}	Maximum output current during electrochemical permeation tests
k	Factor to reduce the cohesive strength in the presence of hydrogen, Eq. (14)
K	Hollomon constant
K_T	Equilibrium constant, Eq. (9)
m	Martensitic laths
n	Hollomon exponent
$\mathcal{N}_A$	Avogadro's number
N_L	number of solvent lattice atoms
N_T	Density of traps
R	Universal gas constant
T	Temperature
t_{lag}	Lag time
u	Displacement
x	Horizontal axis
y	Vertical axis
β	Number of interstitial lattice sites per Fe atom
δ	Separation
Δa	Crack advancement
Δg_b^0	Variation in Gibbs free energy
ε	Strain
ε_ρ	Equivalent plastic strain
θ	Hydrogen coverage
θ_T	Trapping occupancy
ρ	Dislocations
ρ'	Iron density
σ_0	Cohesive strength of the uncharged material
σ_H	Cohesive strength in the presence of hydrogen
σ_{uts}	Ultimate tensile strength
σ_{ys}	Yield stress
Φ	Heating rate

Abbreviations

BCC	Body-centred cubic

CTOD	Crack tip opening displacement
CZM	Cohesive Zone Model
DFD	Discrete Fréchet Distance
FEM	Finite Element Method
HB	Brinell Hardness
HE	Hydrogen Embrittlement
HEDE	Hydrogen Enhanced DEcohesion mechanism
HELP	Hydrogen Enhanced Localized Plasticity mechanism
LLD	Load line displacement
RT	Room temperature
TDA	Thermal Desorption Analysis
TEM	Transmission Electron Microscopy
TTP	Temperature–Time–Precipitation
XFEM	Extended finite element method

experimental data and validated numerical tools to accurately describe the degradation of these materials in the presence of hydrogen. Indeed, Hydrogen Embrittlement (HE) can limit the performance both in terms of fatigue life and fracture toughness, based on different mechanisms discussed in the literature, as the Hydrogen Enhanced DEcohesion (HEDE) model and the plasticity-mediated HE models (Hydrogen Enhanced Localized Plasticity – HELP, Hydrogen-Enhanced Strain-Induced Vacancy HESIV, Adsorption Induced Dislocation Emission – AIDE, and Defactant concept). Comprehensive reviews by Djukic et al. [2] and Dwivedi et al. [3] suggest that combinations of different mechanisms may occur based on the different chemical compositions of the steels.

Hydrogen can diffuse through the metallic lattice, but it can also be trapped in various sites that can interact via chemical equilibrium. Traps are usually characterized by two parameters: binding energy E_b and trap density N_T. Researchers classify the traps into two categories, e.g. reversible or irreversible traps, based on the activation energy for trapping/detrapping. The threshold for diffusible trapping sites is often identified as 30 kJ/mol, while very strong or irreversible traps have an activation energy greater than 60 kJ/mol [4]. The type of traps and their interaction with the hydrogen in the steel lattice depend on the microstructure. Their type and density can deeply influence the macroscopic mechanical behaviour under static and fatigue loads, ultimately resulting in the HE phenomenon. According to Dadfarnia et al. [5], the diffusion transient can be deeply affected by the trap density and types. The authors suggested introducing traps into the material microstructure to immobilize or trap absorbed hydrogen, thereby limiting the amount of hydrogen that contributes to the embrittlement process during the transient. For instance, the effect of molybdenum and vanadium addition was discussed by Peral et al. [6] comparing V-free and V-added steels, suggesting a path to improve the mechanical properties. More recently, Liu et al. [7] increased trapping capacity by adding molybdenum and creating Ti-Mo carbides which reduce the diffusion energy barrier between the carbon vacancies in the metal carbide bulk. These works underline the key role of traps; indeed, they affect hydrogen diffusion during the transient, influence the time to reach the steady state, and modulate the rate of the hydrogen supply to the fracture process zone of the crack front.

The literature faced HE not only through experimental but also with numerical studies, focusing on the macroscale and simulating the fracture toughness degradation in the presence of hydrogen. Different numerical techniques have been successfully implemented based on the Finite Element Method (FEM), e.g., the Cohesive Zone Models (CZM) [8,9], the phase-field models [10–12], the EXtended Finite Element Method (XFEM) [13]. Some recent studies [14–16] started discussing the role of traps; however, these models require many inputs that are not always readily available. These inputs are frequently collected from experimental data in the literature, sometimes obtained from tests on different alloys. This can lead to discrepancies in numerical estimations and misinterpretations of the effects of traps.

To the best of the authors' knowledge, no numerical paper has attempted to simulate HE and the trapping effect using only experimental inputs derived from tests specifically designed for this purpose, following a systematic procedure to inform the numerical model.

The present study focuses on the simulation of a CrMo steel using a CZM. The first part of the work presents and summarizes targeted experimental tests that collect all necessary inputs for the simulation of a fracture toughness test, both in the absence and presence of hydrogen. The second part presents the results of the numerical simulation, discussing the ability of the model to identify the process zone and the macro-mechanical behaviour, while also providing an overview of the hydrogen concentrations in the lattice and traps ahead of the crack tip.

2. Material

The focus is on a low-alloy ferritic steel, namely 2.25Cr1Mo steel, which is classified as Grade 22 in ASTM A387 [17]. In previous works [6,18], the authors described the results of microstructural characterization and mechanical tests performed in the presence of hydrogen. These findings will be summarized here and in the next section.

Under typical working conditions, quenching and tempering are the standard thermal treatments for this steel to achieve good mechanical properties, especially regarding strength and toughness. The heat treatment process involves heating the steel to 940 °C for 3 h, followed by water quenching and tempering at 690 °C for 30 h, before allowing it to cool in air. This tempering temperature simulates a Post Weld Heat Treatment (PWHT), which aims to relax the microstructure to enhance both strength and toughness.

The resulting microstructure is tempered martensitic with elongated carbides precipitated during the tempering stage. They are homogeneously distributed along grains and martensitic packets, blocks and lath interfaces, with a similar average thickness of about 1 μm [19]. The mixed carbides identified include M_7C_3, M_2C and $M_{23}C_6$. The prior austenite grain boundary measures approximately 25 μm. Table 1 shows the main mechanical properties.

3. Methods

3.1. Experimental methods

The hydrogen pre-charging process is performed in a high-pressure hydrogen reactor at 19.5 MPa, 450 °C and 21 h of exposure time. The samples are then cooled for 1 h until reaching 85 °C at the same hydrogen pressure. Following cooling, the samples are removed from the reactor and stored in liquid nitrogen to minimize hydrogen loss until testing occurs.

This section is dedicated to the experimental testing campaign carried out to gather all the inputs for the FE model. Table A1 in the Appendix summarizes all the performed tests and measured quantities.

3.1.1. Thermal desorption analysis

Thermal Desorption Analyses (TDA) are conducted on cylindrical pins with a diameter of 10 mm and a length of 30 mm using a hydrogen analyser LECO DH603 to detect potential hydrogen trapping sites. The average total hydrogen concentration is about 0.6 wppm, while 0.2 wppm remains strongly trapped in the microstructure after a long exposure time at room temperature (RT) (Fig. 1.a). Hence, approximately less than 0.4 wppm of hydrogen can diffuse out from the lattice and reversible trapping sites at RT.

The trap activation energy (E_a) is determined by detecting the released hydrogen as a function of the heating rate (Φ_i) [20]. TDA profiles of Fig. 1.b evidence three distinct peaks corresponding to three trap types. The trap binding energy (E_b) is then calculated, assuming:

$$E_a = E_b + E_L \tag{1}$$

where E_L is the activation energy of hydrogen diffusion in the BCC iron lattice, which has a value of 4.15 kJ/mol [21]. Fig. 1.c shows the data fitting and Table 2 provides the resulting binding energies for each trapping site, which are consistent with existing literature data [22]. The complex microstructure of martensitic steel hinders a comprehensive characterization of the different hydrogen trapping sites. In quenched and tempered microstructures, dislocations rearrange into cells, and these cell interfaces correspond to lath, packet, and block martensite interfaces, as well as their interaction with the PAGB. Additionally, most carbides precipitate here, making it difficult to separate the trapping contributions from all these microstructural features. After TDA, we postulate that dislocations, martensitic interfaces, and metal carbides appear to act as potential hydrogen trapping sites.

3.1.2. X-ray diffraction

The dislocation (ρ) density, estimated by the X-ray diffraction technique [18], and the trapping density sites corresponding to dislocations are displayed in Table 3. The density of traps related to dislocation is estimated with a lattice parameter $\overline{a}$ equal to 0.2867 nm from Eq. (2) [23]:

$$N_T^{\rho} = \frac{\sqrt{2}}{\overline{a}}\rho \tag{2}$$

These experimental findings can be fitted with an interpolating exponential curve, as suggested in [24]. The resulting curve has the following equation:

$$logN_T^{\rho} = 24.4591 - 0.8571exp(-50 \bullet \varepsilon_p) \tag{3}$$

where ε_p is the equivalent plastic strain. The trend is reported in Fig. 2.

In comparison with the previous fitting curves found in the literature works, this study opts to fit the experimental data with a very sharp trend that flattens rapidly, based on the available experimental data. This is a feature of the 2.25Cr1Mo steel; the N_T vs ε_p curves cannot be generalized with a universal trend, but they should be customized based on the tested steel. Indeed, these curves play an important role in numerical analysis where they should be considered as an input, if known from experimental data, or calibrated if unavailable.

Fig. 2 shows that there could be an almost four-order-of-magnitude difference when comparing the results available in the literature to estimate N_T as a function of the equivalent plastic strain. Hence, Eq. (3) will be implemented in the numerical models presented in Section 3.2.

Table 1
Mechanical properties of the 2.25Cr1Mo steel. Hollomon's parameters are given for the true stress–strain curve.

Hollomon's law: $\sigma_t = K \cdot \varepsilon_{pt}^n$		σ_{ys}	σ_{uts}	A	HB
K (MPa)	n	(MPa)	(MPa)	(%)	
862	0.12	430	594	27	170

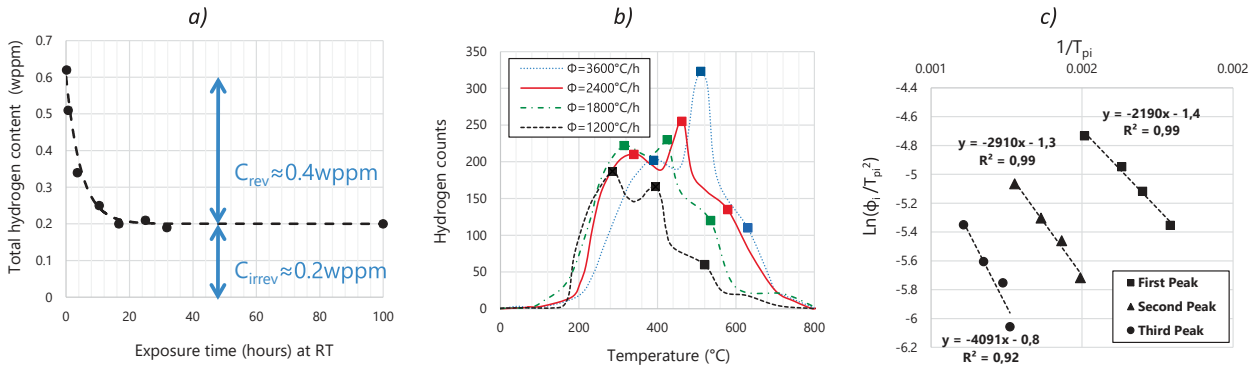

Fig. 1. (a) Hydrogen desorption curve in pins with 10 mm diameter at room temperature, (b) TDA profiles at the different heating rates (Φ_i); (c) Data fitting to determine the activation energy [19].

Table 2
Activation (E_a) and binding (E_b) energies for the different trapping site of the 2.25Cr1Mo steel [19].

E_a (kJ/mol)	E_b (kJ/mol)	Peak	Trapping site
34.00	29.85	3rd	Dislocations
24.40	20.25	2nd	Martensitic interfaces
18.20	14.05	1st	Metal carbides

Table 3
Dislocation density level for different equivalent plastic strains and density of traps corresponding to dislocation [18].

	Un-stressed	$\varepsilon_p = 10$ %	$\varepsilon_p = 20$ %	$\varepsilon_p = 30$ %
ρ (sites/m^2)	$8.1 \cdot 10^{13}$	$5.9 \cdot 10^{14}$	$5.2 \cdot 10^{14}$	$5.9 \cdot 10^{14}$
N_T^{ρ} (sites/m^3)	$4.0 \cdot 10^{23}$	$3.0 \cdot 10^{24}$	$2.6 \cdot 10^{24}$	$3.0 \cdot 10^{24}$

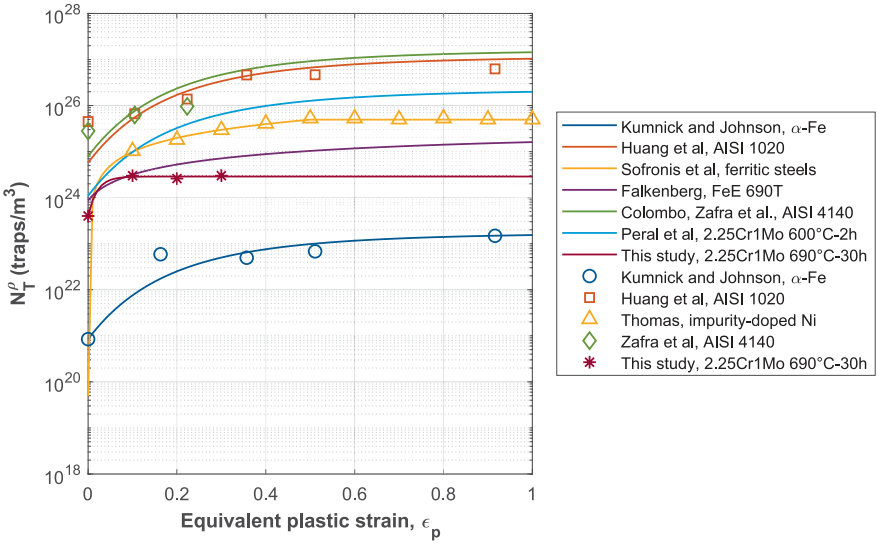

Fig. 2. Dislocation trap density N_T^{ρ} as a function of the equivalent plastic strain ε_p. Analytical laws: Krom et al. [25], Huang et al. [26], Sofronis et al. [27], Falkenberg [28], Colombo et al. [29]. Experimental data: Kumnick and Johnson [24], Huang et al. [26], Thomas [30], Zafra et al. [31] and Peral et al. [32].

3.1.3. SEM and TEM observations and TTP curves

The density of the second type of traps in Table 2, e.g. hydrogen trapped in the interface carbide-matrix, follows Eq. (4) [33]:

$$N_T^c = \left(\sum_j \pi \cdot d_j^2 \cdot f_j\right) \cdot \frac{4}{\bar{a}^2} \cdot \frac{1}{L^3} \tag{4}$$

where j is the variable corresponding to each carbide, d is the size of the carbide, f is the volume fraction of the carbide, $\bar{a}$ is the lattice parameter previously defined, and L is the average distance between the carbide particles, estimated from Transmission Electron Microscopy (TEM) images as approximately 125 nm. The values of the d and f parameters are obtained from Temperature–Time–Precipitation (TTP) curves and JmatPRO software after tempering at 690 °C for 30 h. Table 4 summarizes their values, allowing for the estimation of $N_T^c = 1.25 \cdot 10^{24} sites/m^3$ as from Eq. (4).

The density of the third type of traps can be estimated according to Eq. (5) for hydrogen trapped in martensitic interfaces [34]:

$$N_T^m = \frac{b}{D_g} N_L \tag{5}$$

where b is the Burgers vector (0.248 nm for BCC iron), D_g is the grain size equal to 25 μm, and N_L is the number of solvent lattice atoms [35]:

$$N_L = \frac{\mathcal{N}_A \beta \rho'}{A_r} \tag{6}$$

where $\mathcal{N}_A$ is the Avogadro's number, β is the number of interstitial lattice sites per Fe atom (6, under the hypothesis of occupation of the tetrahedral sites by hydrogen atoms at room temperature), ρ' is the iron density, and A_r is the molar mass of Fe. It results $N_T^m = 5.84 \bullet 10^{24} sites/m^3$.

Eventually, the total density of traps N_T can be estimated as the sum of the three contributions:

$$N_T = N_T^o + N_T^m + N_T^c \tag{7}$$

3.1.4. Electrochemical permeation experiments

Electrochemical permeation experiments (EPE) are carried out to study the interaction between hydrogen atoms and steel microstructure. Hydrogen permeation experiments are performed at 1 mA/cm^2. Fig. 3 shows the permeation curves, whilst the obtained results are summarized in Table 5.

It is important to mention that $N_{T,0}^{EPE} = 2.3 \bullet 10^{24}$sites/m^3, e.g. the trap density in the initial unstressed condition, obtained from these permeation tests has the same order of magnitude as the corresponding value estimated from the TDA. Indeed, from Eq. (7) and considering all the potential trapping sites, the estimated value is $N_{T,0}^{TDA} = 7.49 \cdot 10^{24}$sites/m^3. For the numerical simulations, the more detailed results of N_T obtained from the TDA are accounted for the different traps; on the other hand, the results of diffusivity D_L and initial hydrogen concentration in the lattice $C_{L,0}$ from the electrochemical permeation experiments will be considered as inputs of the finite element analysis.

3.1.5. Fracture toughness tests

Fig. 4 shows the results of the fracture toughness tests performed following ASTM E1820-23 standard on C(T) specimens of 12 mm thickness [36]. Tests are performed in uncharged and hydrogen precharged conditions. Besides, the precharged specimens are tested at 1 and 0.01 mm/min; the results of these two test speeds evidence the effect of time lag allowing for the hydrogen to flow at the crack tip. Indeed the curves, both in terms of load vs. load line displacement LLD (Fig. 4.a) and crack tip opening displacement CTOD vs. crack advancement Δa (Fig. 4.b), experience a decrease in fracture toughness, hence a deep increase of the percentage embrittlement index EI, Eq. (8):

$$EI = \frac{\left(CTOD_{Uncharged} - CTOD_{Pre-charged}\right)}{CTOD_{Uncharged}} \bullet 100 \tag{8}$$

where $CTOD_{Uncharged}$ and $CTOD_{Pre-charged}$ are respectively the measured crack tip opening displacements evaluated without and with internal hydrogen. Table 6 summarizes the results of the toughness tests, with the details of the $CTOD$ values in correspondence of the 0.2 mm and 1.5 mm offset lines, e.g. for these two values of crack propagation, typically corresponding to the initiation and to the propagation (exclusion line) according to the ASTM E1820 standard. Correspondingly, the EI is calculated for both these values of the

Table 4
Parameters estimated from TTP curves, used in Eq. (4).

Carbide	d, size (nm)	f, volume fraction (%)
M_7C_3	30	0.4
$M_{23}C_6$	20	3.1

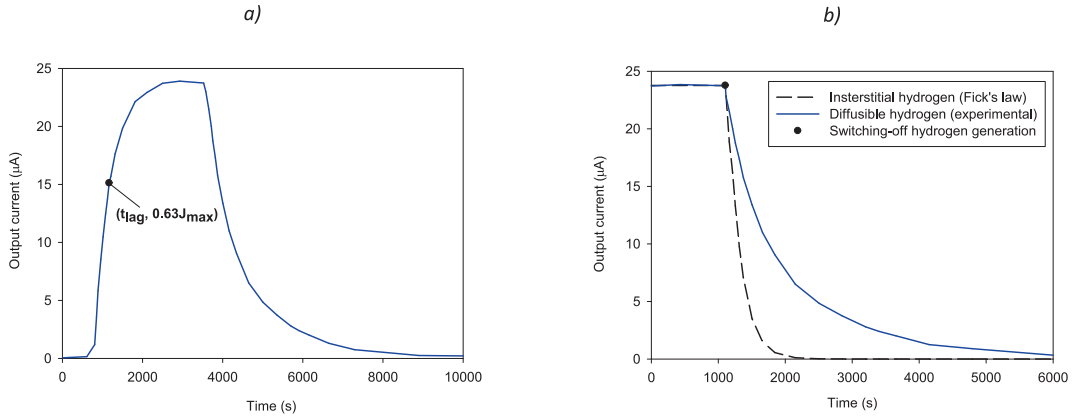

Fig. 3. (a) Electrochemical permeation curve and (b) hydrogen desorption.

Table 5

(a) Parameters calculated from the permeation experiment according to ASTM G148 that corresponds to the un-stressed state; $N_T = \frac{\langle C \rangle}{3}\left(\frac{D_L}{D_{app}} - 1\right)$.

(b) Hydrogen states in the un-stressed condition. $\langle C \rangle = \frac{C_{app}}{2} = C_L + C_{rev} + C_{irrev}$.

a. J_{max} (μA)	t_{lag} (s) in 0.63J_{max}	D_{app} (m^2/s)	C_{app} (wppm)	D_L (m^2/s)	$N_{T,0}^{EPE}$(sites/m^3)
23.8	1168	$1.4{\cdot}10^{-10}$	2.0	$5.5{\cdot}10^{-10}$	$2.3{\cdot}10^{24}$

b. $C_{L,0}$ (wppm)	C_{rev} (wppm)	C_{irrev} (wppm)	C_T (wppm)	θ_T (%)
≈ 0.1–0.15	≈ 0.2	0.7	0.9	≈ 90

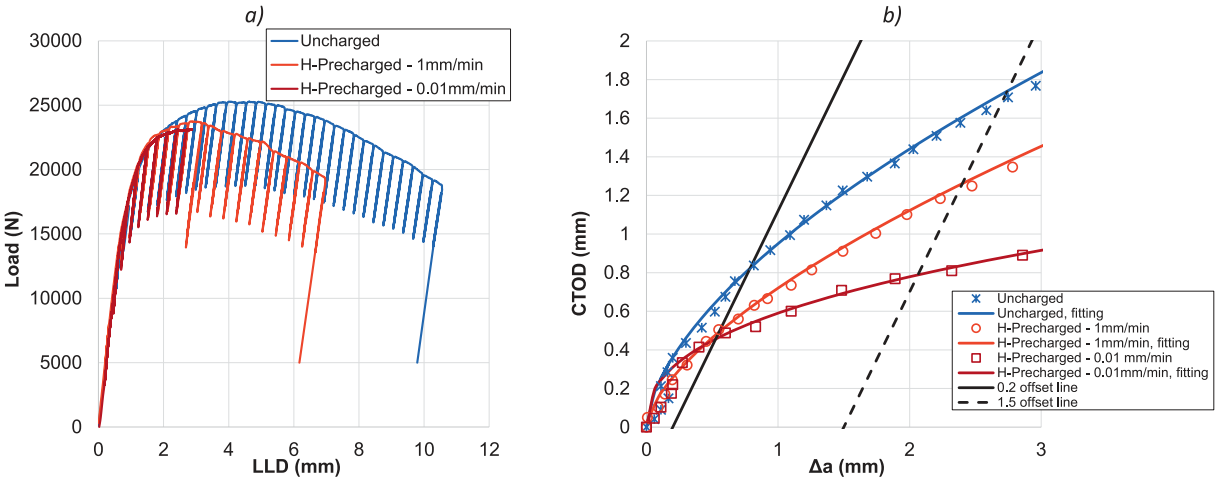

Fig. 4. Results of the fracture toughness tests in uncharged and precharged configurations. (a) Load vs. load line displacement (LLD), and (b) crack tip opening displacement (CTOD) vs. crack advancement Δa. Fitting curves are plotted with the parameters C_1 and C_2 of Table 6.

CTOD. It is worth noting that the initiation is not deeply influenced by the test speed, rather by the simple presence of hydrogen, e.g. the *EI* is similar comparing the $CTOD_{0.2}$ in Table 6.b. On the other hand, the effect of the test speed is much more evident in the case of the $CTOD_{1.5}$. At 1 mm/min, the value of *EI* based on $CTOD_{1.5}$ decreases with respect to the $CTOD_{0.2}$; due to the high displacement rate, hydrogen has little time to diffuse at the tip. At 0.01 mm/ min, *EI* increases between 0.2 and 1.5 mm propagation; indeed, the time that hydrogen needs to move towards the new crack tip starts playing its role by virtue of its apparent diffusivity.

Part of the parameters reported in Table 6 are used as inputs for the numerical simulations, such as the test rate for the precharged tests, and the load line displacement (*LLD*) that is set as a boundary condition. Other parameters as the *CTOD* and the time to reach the crack advancement $\Delta a = 3$ mm are direct outputs of the simulations, which, once compared with these experimental values, allow for

Table 6
Fracture toughness results: a) CTOD and Δa value; and b) other experimental parameters.

a)

Test condition	Test rate (mm/min)	$CTOD_{0.2}$ (mm)	$\Delta a_{0.2}$ (mm)	$CTOD_{1.5}$ (mm)	$\Delta a_{1.5}$ (mm)
Uncharged	1	0.824	0.788	1.741	2.743
H-Precharged	1	0.492	0.551	1.261	2.401
H-Precharged	0.01	0.456	0.526	0.788	2.062

b)

Test condition	Test rate (mm/min)	Time (s) when $\Delta a = 3$ mm	*LLD* (mm) when $\Delta a = 3$ mm	$CTOD = C_1 \cdot \Delta a^{C2}$		*EI* (%)	
				C_1	C_2	$CTOD_{0.2}$	$CTOD_{1.5}$
Uncharged	1	841	8.1	0.95	0.60	–	–
H-Precharged	1	528	6.5	0.72	0.64	40	28
H-Precharged	0.01	13,268	4.6	0.59	0.40	45	55

the validation of the numerical tool as will be described in the next Section 3.2.

Fig. 5 shows the fracture surfaces corresponding to different test conditions. In the absence of hydrogen, see Fig. 5.b, the fracture micro-mechanism is fully ductile, characterized by Micro Void Coalescence (MVC). However, in the presence of internal hydrogen, the fracture micro-mechanism becomes more brittle. Near the notched region, areas exhibiting quasi-cleavages (QC), which indicate martensitic lath decohesion and secondary cracks, are clearly visible (see Fig. 5.d and f). Based on the thermal desorption analysis, martensitic interfaces act as reversible hydrogen trapping sites, promoting hydrogen-enhanced decohesion along the interfaces.

For the highest test speed, Fig. 5.c reveals a fracture surface that is more brittle at the crack tip for about 0.2 mm, e.g. corresponding to $CTOD_{0.2}$. When crack propagates, the morphology is more ductile. On the other hand, at the lowest test speed, Fig. 5.e shows a fully brittle fracture surface because more hydrogen is attracted at the new position of the crack tip. These observations align well with the CTOD and *EI* data in Table 6.b.

The fracture surfaces and the results of the experimental tests discussed in this section suggest that the active mechanisms for hydrogen embrittlement of this 2.25Cr1Mo steel quenched and tempered at 690 °C for 30 h are not straightforward. Instead, there is a synergic effect of the two main HE mechanisms of HELP mediated HEDE. This dual mechanism was identified by Novak et al. [37] for the martensitic steel AISI 4340 (austenized at 870 °C for 1 h, oil quenched and tempered at 200 °C for 2 h). It suggests a transition from the strain-controlled purely ductile fracture by MVC in non-charged samples to a brittle stress-controlled intergranular (IG) fracture ahead of the notch tip in charged samples. Nagao et al. drew similar considerations [33,38] on a martensitic modified AISI 4140 steel. They suggested that, in parallel to the HEDE mechanism acting at the carbide-matrix interface, the brittle IG fracture occurs because of hydrogen transported by dislocations. This HELP mechanism further increases the hydrogen concentration at the carbides and other dislocation barriers, enhancing the HEDE mechanism.

This synergic effect suggests that HELP is a critical mechanism to reach a concentration sufficient to activate decohesion, e.g. the HEDE mechanism. A thorough review of the combination and synergy of these two mechanisms is given in Section 2.2 of the review by Djukic et al. [2].

3.2. Numerical methods

Supposing i-th different types of traps present in the steel microstructure, it is possible to define different equilibrium constants K_T^i through Eq. (9), based on Oriani's equilibrium theory [39] and proposed in its multi-trapping formulation by [5]:

$$K_T^i = exp\frac{E_b^i}{RT} \tag{9}$$

where R = 8.314 J/mol•K is the universal gas constant, and T is the absolute temperature. For each trapping site, the hydrogen trap concentration C_T^i is given by:

$$C_T^i = \frac{N_T^i K_T^i C_L}{\left(K_T^i - 1\right) C_L + N_L} \tag{10}$$

These equations imply that hydrogen atoms in both the trapping sites and the lattice are locally in equilibrium, assuming rapid trapping and detrapping kinetics.

For the specific steel under investigation, three types of traps are identified by the experimental TDA, e.g. carbides, martensitic laths, and dislocations (i = 3, see Table 2). Hence, the total hydrogen concentration stored in the traps is expressed as the sum of the three contributions:

$$C_T = C_T^p + C_T^m + C_T^c \tag{11}$$

Once the hydrogen in the traps is estimated, then the total hydrogen content can be calculated as the sum of the hydrogen in the

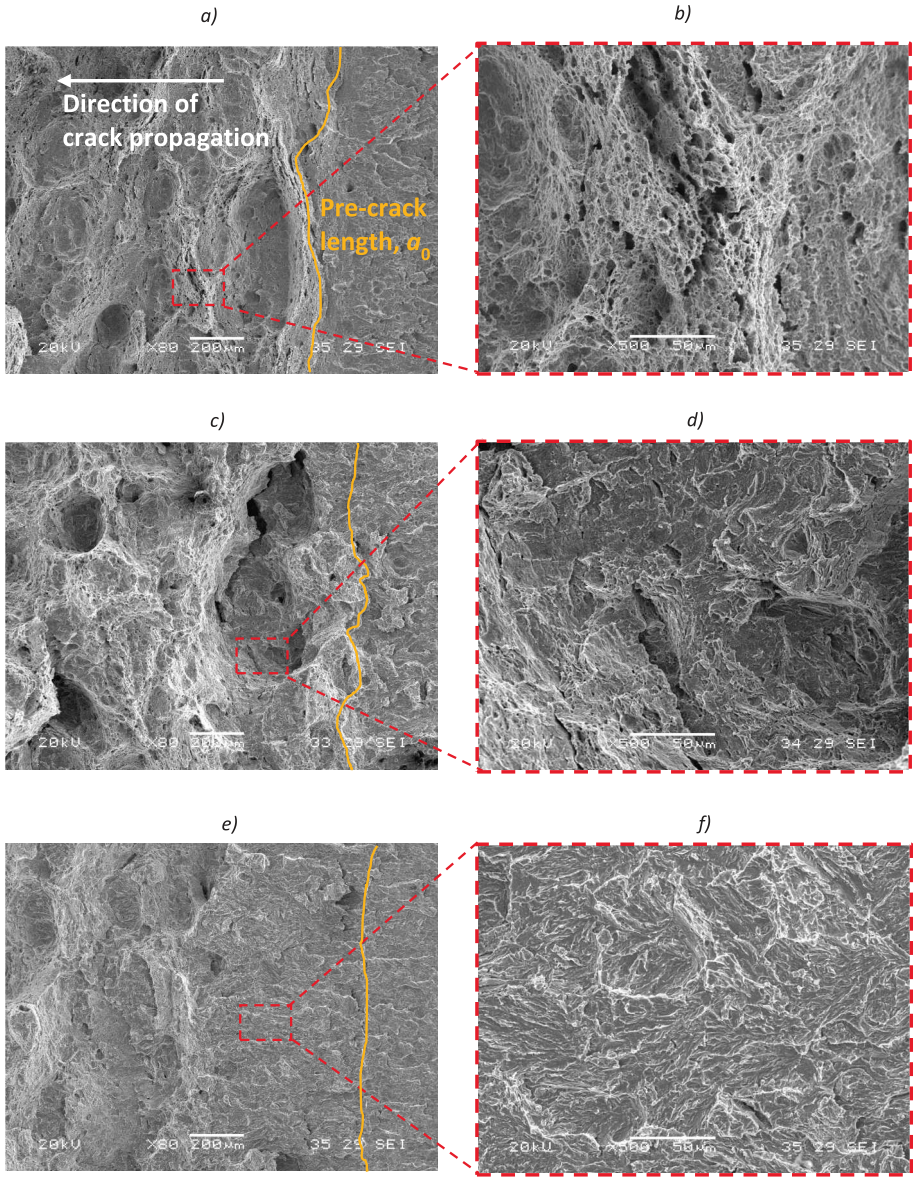

Fig. 5. Fracture surfaces. (a) and (b) Uncharged condition; (c) and (d) Hydrogen precharged condition and tested at 1 mm/min; (e) and (f) Hydrogen precharged condition and tested at 0.01 mm/min.

lattice and in the traps:

$$C = C_L + C_T \tag{12}$$

The hydrogen diffusion and the elastoplastic behaviour of the material are coupled. The initial framework is the open-source Polihydra code, previously implemented by the authors with the software ABAQUS by Dassault Systèmes, originally designed to consider only dislocation traps [9]. This open-source code, available at [40], was used in past works to simulate HE of other steels such as AISI 4130 [41], AISI 4140 [29], as well as the same 2.25Cr1Mo steel [32] but austenitized at 940 °C for 30 min, quenched in water and finally tempered at 600 °C for 2 h. For all these steels, the only active fracture mechanism in the presence of hydrogen was the HEDE; hence, the Polihydra framework was appropriate.

For the thermal treatment at 690 °C currently being examined, the results of the TDA and the fracture surfaces of Fig. 5 indicate that other traps beyond dislocations are present in the martensitic microstructure. Therefore, for the present study, it is necessary to implement Eqs. (9)–(11) and embed them in the user subroutine UVARM of the code. This step is mandatory to simulate the behaviour of the steel correctly and to catch the failure mechanism enhancing crack propagation.

An initial hydrogen concentration $C_{L,0}$ of 0.2 wppm is assumed to be uniformly distributed in the solid elements, setting null

hydrogen flux as a boundary condition at the exposed surfaces, e.g. insulation. Indeed, hydrogen leaving the specimen during the testing time is limited, as from the experimental results obtained from similar steels in [42].

The numerical 2D framework is based on a Cohesive Zone Model (CZM), where cohesive elements are placed at the specimen's ligament. Their traction-separation law (TSL) is implemented with the tabular softening formulation available in ABAQUS, which allows for a theoretically unlimited number of independent parameters and enables the creation of different TSL shapes that approximate the non-linear fracture process [43]. Being the TSL a phenomenological law, its formulation is material-specific and independent of the geometry. For instance, Schwalbe et al. [44] report a comparison between three calibrated TSL shapes (e.g., partly constant, polynomial, cubic decrease), all capable of fitting the global behavior of both C(T) and M(T) specimens. This observation suggests that different TSL shapes can reproduce the local change in stiffness from the crack initiation up to its propagation, and ultimately catch the global mechanical behavior in terms, for instance, of CTOD-Δa. For the current simulations, a trapezoidal TSL shape [45] is selected, characterized by four independent parameters: the three separations δ_0, δ_1, δ_F and the cohesive strength at the plateau σ_0. In particular, δ_0 delimits the elastic stage, governs the damage initiation based on the maximum strain criterion and is selected to have an initial slope of the TSL as steep as possible, δ_1 identifies the plateau with the plastic stage, and δ_F fixes the final failure with the separation of the cohesive finite element. As a rule of thumb, [44] suggest $\delta_0 \leq 0.05 \bullet \delta_F$ and $\delta_1 \leq 0.75 \bullet \delta_F$.

The calibration of the TSL parameters is carried out with a trial-and-error procedure fitting the experimental CTOD-Δa curve of the uncharged specimen (Table 7). On the other hand, when the simulation in the presence of hydrogen is considered, the total hydrogen concentration C is obtained at each increment of the simulation according to Eq. (12) and is used to decrease the TSL plateau, calculating at first the hydrogen coverage θ from the Langmuir-McLean isotherm [46]:

$$\theta = \frac{C}{C + exp\left(\frac{-\Delta g_b^0}{RT}\right)} \tag{13}$$

where $-\Delta g_b^0$ is the variation in Gibbs free energy between the microstructural interface and the bulk (30 kJ/mol, [47]). Then, the cohesive strength in the presence of hydrogen σ_H is calulated from the cohesive strength of the uncharged material σ_0 following the empirical quadratic polynomial by Jiang and Carter [48]:

$$k = \frac{\sigma_H}{\sigma_0} = 1 - 1.0467 \bullet \theta + 0.1687 \bullet \theta^2 \tag{14}$$

The ratio k describes the strength degradation of the cohesive elements at the ligament of the C(T) specimen and drives crack initiation and advancement over time. Fig. 6 schematizes the geometry, the plane strain mesh, boundary conditions and the degradation process. The simulations are run in displacement control, applying the experimental load line displacement LLD as in Table 6 to the hole (Fig. 6.a). The vertical displacements of the cohesive elements at the symmetry plane are fixed, and their relative horizontal displacements are locked ($u_{x,up} = u_{x,down}$, see Fig. 6.c). The mesh of plane strain and cohesive elements (i.e., CPE4RT and COH2D4 according to ABAQUS identification) is progressively refined in the ligament towards the crack tip, where, after a convergence study considering the concentration target, the smallest element at the crack tip is fixed to 30x30 μm. The element size is chosen based on these purely numerical considerations. The most refined region, with uniform element size, extends 3 mm ahead of the initial crack tip. Beyond this Δa, the specimen can be considered as failed, and the experimental test becomes meaningless. Fig. 6.d plots the TSL degradation according to Eq. (14), as a function of the degradation ratio k, the hydrogen coverage θ and the total hydrogen concentration C. The saturation level corresponds to $k = 0.12$. It is worth noting that, according to the damage formulation implemented in the used framework [9], the damage curves collapse as a function of the separations δ, because they do not depend on the cohesive strength (Fig. 6.e).

Eventually, the outputs of the numerical simulations are post-processed with the software MATLAB by MathWorks.

4. Results

Fig. 7 shows a comparison of CTOD-Δa between the experimental data from fracture toughness tests and their corresponding numerical simulations. It is worth recalling that the uncharged data are used to calibrate the TSL parameters, which are listed in Table 7. The fitting is performed considering the Discrete Fréchet Distance (DFD, [49]) as the parameter to minimize. The calibration shows a good match in the region between the two offset lines, which is of higher interest from the practical mechanical viewpoint, with percentage differences in CTOD ranging from 10 to −0.5 %, see Table 8.

On the other hand, the numerical CTOD-Δa hydrogen precharged data in Fig. 7, at 1 and 0.01 mm/min, represent estimations from the model. The case at 1 mm/min is underestimated, whereas the case at 0.01 mm/min is overestimated, as detailed in Table 8 for both CTOD and Δa. However, the maximum difference in this range is 16 %. This value is supported by the DFD metrics also reported in Table 8.

Table 7
Parameters used to describe the trapezoidal TSL curve of the cohesive elements.

δ_0 (mm)	δ_1 (mm)	δ_F (mm)	σ_0 (MPa)	σ_0/YS
$5.0 \bullet 10^{-4}$	$2.0 \bullet 10^{-2}$	$5.0 \bullet 10^{-2}$	1800	4.19

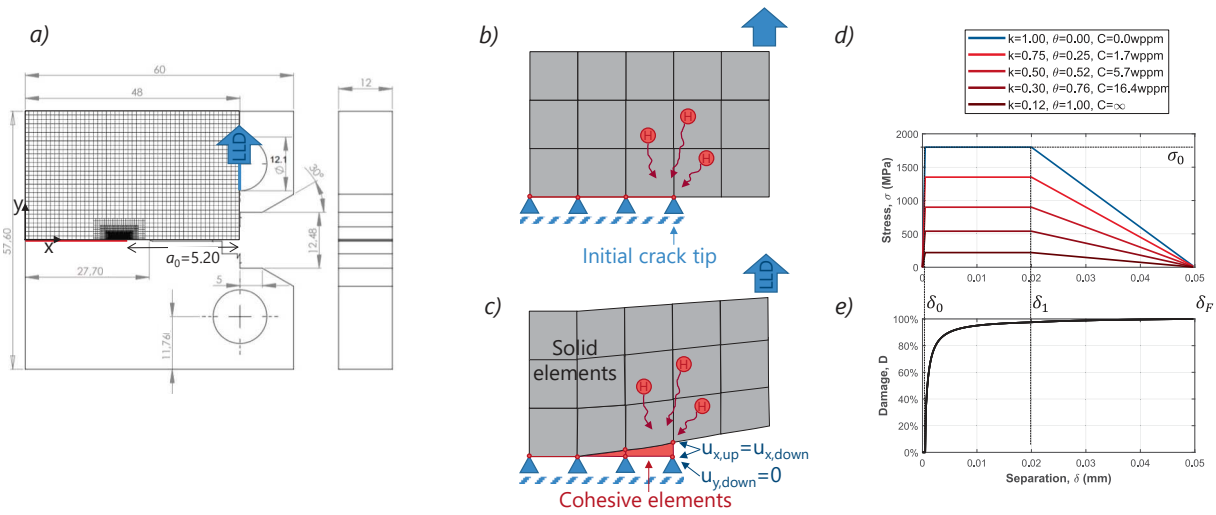

Fig. 6. a) C(T) geometry and meshed region; b) schematization of the undeformed shape; c) schematization of the deformed shape; d) TSL degradation as a function of hydrogen; e) damage law.

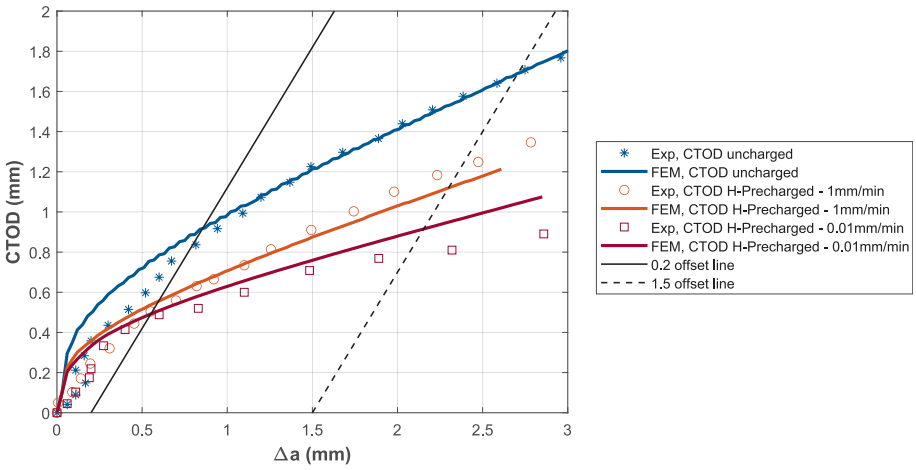

Fig. 7. CTOD-Δa curves from the numerical simulations compared with the experimental toughness data of Fig. 4.b, for uncharged and pre-charged specimens.

Table 8
Numerical CTOD and Δa values at different test speeds and in correspondence of two offset lines (e.g., 0.2 and 1.5 mm) of the CTOD-Δa curves, and comparison with the corresponding experimental data of Table 6.a.

Test condition	Test rate (mm/min)	Numerical				Difference w.r.t. experimental (%)				
		$CTOD_{0.2}$ (mm)	$\Delta a_{0.2}$ (mm)	$CTOD_{1.5}$ (mm)	$\Delta a_{1.5}$ (mm)	$CTOD_{0.2}$	$\Delta a_{0.2}$	$CTOD_{1.5}$	$\Delta a_{1.5}$	Discrete Fréchet Distance (mm)
Uncharged	1	0.921	0.87	1.696	2.73	10.4	11.8	−0.5	−2.6	1.0128
H-Precharged	1	0.557	0.60	1.123	2.31	8.8	13.2	−3.8	−11.0	1.5367
H-Precharged	0.01	0.498	0.57	0.917	2.16	8.4	9.2	4.7	16.3	2.1286

This result can be considered satisfactory, given that the numerical simulations were run using all experimental parameters as inputs, whose values can be affected by measurement errors. Besides, the initial concentration in the numerical simulation is considered uniform throughout the specimen, including its thickness. However, this assumption may not be realistic in the experimental tests due to the three-dimensional nature of the problem. Hence, one limitation of this approach is its numerical bidimensionality. Due to the complexity of these simulations and the long computational time, few authors addressed the crack propagation problem with 3D models. Notable examples include Alvaro et al. [50] with cohesive elements, Suman et al. [51] with

XFEM and Kristensen et al. [52] with phase-field modelling. Currently, the focus of this research is to continue working with a 2D model, to explore its potentials and obtain the most promising results from this relatively simple approach.

Fig. 8 shows the concentration fields near the crack tip, at the time increment corresponding to the failure of the first cohesive element, at 1 and 0.01 mm/min. C_L, C_T^c, C_T^m are proportional to each other and driven by the only hydrostatic stress gradient, as from Eqs. (9) and (10). A peak in concentration C_L is observed ahead of the crack tip (Fig. 8.a and b). The concentrations in the carbides and the martensitic laths are much smaller than in the lattice, which exhibits the highest concentration overall. Indeed, C_T^ρ is driven by the equivalent plastic strain field, experiencing its maximum near the crack tip and rapidly decreasing along the ligament (Fig. 8.c and d). Eventually, C is the sum of the four contributions (Fig. 8.e and f).

There is a notable effect of the test speed when comparing all the concentration fields. Indeed, the concentrations that are dependent on the hydrostatic stress gradient exhibit differences due to the varying time lag in hydrogen diffusion at the tip.

Fig. 9 plots the trends of the concentrations as a function of the distance from the initial crack tip position. The values are normalized based on C_{L0}, the initial lattice concentration, which is set as the input parameter for the simulation. The subfigures evidence the normalized concentrations at the failure of the first cohesive element (Fig. 9.a and b), the 0.2 offset line (Fig. 9.c and d) and the 1.5 offset line (Fig. 9.e and f), respectively.

The trend of the concentration in the lattice, C_L, is quite smooth and exhibits a peak ahead of the crack tip, where the hydrostatic stress gradient is maximum. The concentrations in the carbides and martensitic laths are three and two orders of magnitude lower than C_L, respectively, at every time increment in the simulations. The C_T^ρ trend experiences a peak comparable with the lattice concentration in the first cohesive element and for both the testing speeds (Fig. 9.a and b), suggesting that the crack propagation occurs via the HELP mediated HEDE mechanism. From these outputs, it seems that dislocations primary influence of the traps' content, while the contributions from carbides and martensitic laths are limited.

When monitoring the crack propagation at 0.2 and 1.5 offset lines (Fig. 9.c–f), the trend of hydrogen content in the dislocations

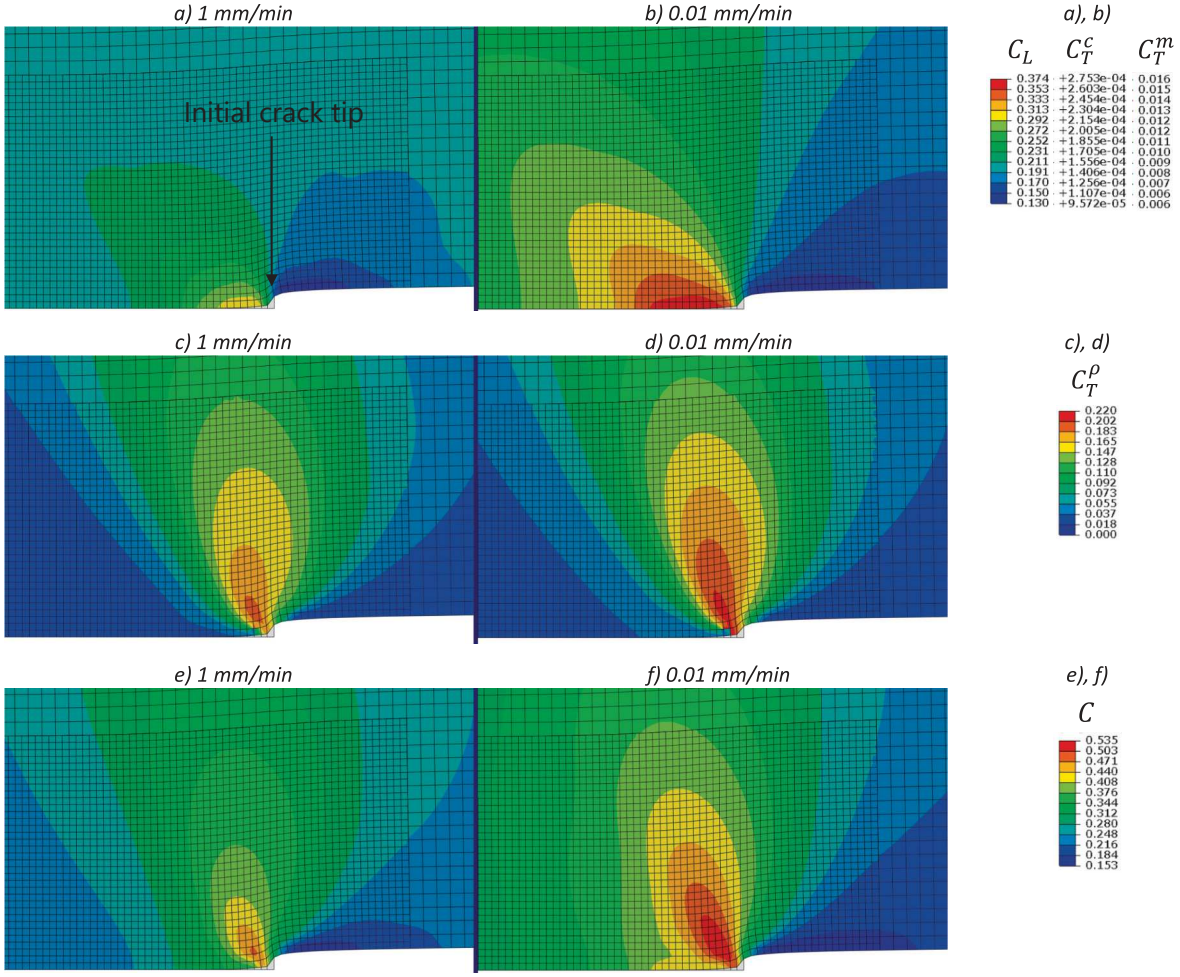

Fig. 8. Concentration fields at failure of the first cohesive element, at different test speeds: (a)-(c)-(e) 1 mm/min; (b)-(d)-(f) 0.01 mm/min. Fields and legends: (a) and (b) C_L, C_T^c, C_T^m, proportional to each other; (c) and (d) C_T^ρ; (e) and (f) C. Unit: wppm.

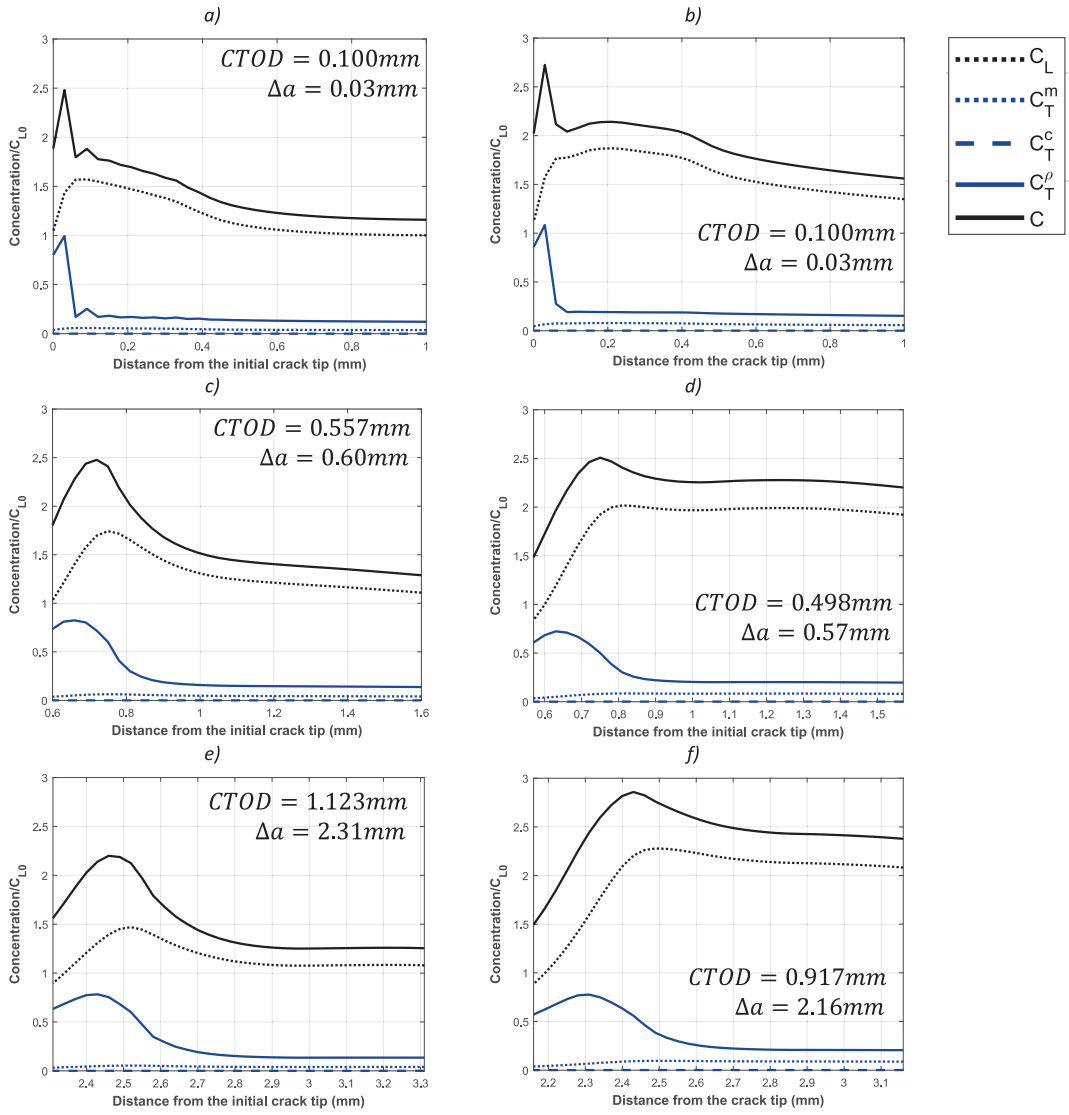

Fig. 9. Trends of normalized hydrogen concentrations along the ligament, at different test speeds: a)-(c)-(e) 1 mm/min; (b)-(d)-(f) 0.01 mm/min. Considered time increments at: (a) and (b) failure at the failure of the first cohesive element; (c) and (d) crack initiation at 0.2 offset line; (e) and (f) crack propagation at 1.5 offset line.

becomes smoother and experiences a peak ahead of the crack tip in its new position. The C_T^{ρ} peak is closer to the crack tip than the C_L peak. As a result, the total hydrogen concentration reflects these two contributions, leading to a wavy trend.

At the testing speed of 1 mm/min the total concentration peak decreases from 0.2 to 1.5 offset line, see Fig. 9.c and d. This observation explains the decrease in the *EI* at $CTOD_{0.2}$ in Table 6.b and the fracture surface of Fig. 5.c. Thus, these experimental and numerical results are consistent with each other. The other way round, at 0.01 mm/min, Fig. 9.d and e display an increase in the total concentration peak, which agrees with the increase in the *EI* at $CTOD_{1.5}$ in Table 6.b and with the brittle fracture surface of Fig. 5.e. Therefore, the numerical approach effectively quantifies the influence of test speed on hydrogen concentration, which is reflected in both the experimental mechanical results and the fractographic outcomes.

Based on these considerations, it is possible to focus on the C/C_{L0} trends of Fig. 9, which are the most important numerical outputs used to decrease the TSL law and degrade the cohesive elements at the ligament. From this viewpoint, it is suggested to monitor three main quantities during crack advancement: 1) the total concentration at the crack tip, C_{tip}; 2) the total concentration peak, C_{peak}; and 3) its distance with respect to the actual position of the crack tip, d_{peak}. Fig. 10.a shows a scheme to identify these quantities, while their plots are given in Fig. 10, b-c-d as a function of crack advancement Δa, for the two testing speeds. The trends are interpolated with MATLAB exponential or smoothing splines for better visibility.

At the initiation stage (when $\Delta a = 0$), the hydrogen concentration at the tip, C_{tip} (Fig. 10.b), is 2.48 and 2.72 times the initial C_{L0} for the speeds of 1 mm and 0.01 mm/min, respectively. At this stage, the C_{tip}/C_{L0} trend is very steep and the difference between the two

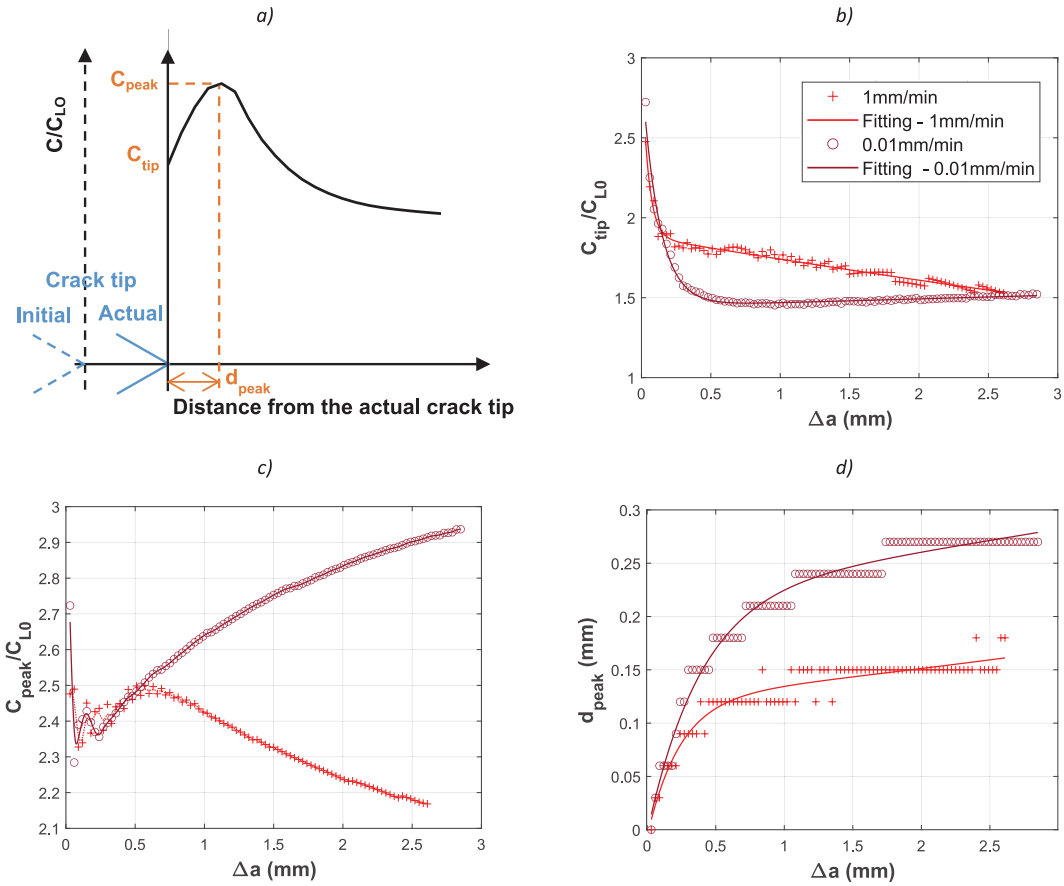

Fig. 10. (a) Scheme of the three focussed parameters, and trends of: (b) normalized total hydrogen concentration at the tip; (c) normalized total hydrogen concentration at the peak; (d) distance of the peak concentration with respect to the crack tip. Trends are ploted as a function of the test speed (e.g., 1 and 0.01 mm/min). The fitting is obtained with (b)-(d) exponential and (c) smoothing splines.

test speeds seems not relevant, as evidenced by the *EI* from $CTOD_{0.2}$ in Table 6.b, e.g. 40 and 45 %. It can be deduced that a total hydrogen concentration of approximately 2.5 C_{L0} is critical to initiate the failure process, regardless of time. Notably, after this point, there is a marked difference between the two test speeds. Indeed, when the crack propagates, hydrogen diffusion as a function of time has a predominant role and changes the concentration trend, which is then macroscopically visible in the CTOD-Δa curve. The critical concentration for the crack to propagate is higher at 1 mm/min, while it rapidly flattens to 1.5 C_{L0} at 0.01 mm/min. This 1.5 C_{L0} value also serves as the asymptotic value at $\Delta a = 2.5$ mm when the crack is long. Therefore, the plot of Fig. 10.b should be interpreted as the critical hydrogen concentration plot, or, in other words, the threshold for crack initiation and propagation along the ligament. This numerical result aligns with the experimental observation of the *EI* from $CTOD_{1.5}$ in Table 6.b, which reports values of 28 and 55 % at 1 and 0.01 mm/min, respectively.

The second point of focus on is the peak value ahead of the actual crack tip, illustrated in Fig. 10.c. The peak values are similar between the two testing speeds at the beginning of the propagation, with values slightly higher for 0.01 mm/min. Here, plasticity and HELP mediate the HEDE mechanism and the failure phenomenon. However, when the crack exceeds a length of 0.5 mm the C_{peak} trend at 0.01 mm/min becomes up to 50 % higher than at 1 mm/min, as visible also in Fig. 9.e,f. This plot suggests that higher speeds result in lower peak concentrations, but nearer to the actual crack tip position. Vice versa, when increasing the test speed, the peak is higher and moves away from the crack tip, drawing hydrogen to the next position of the tip and accelerating the propagation. This mechanism is intensified at longer crack lengths by the C_L and the hydrostatic stress gradient, rather than by traps, as evidenced in Fig. 9.e and f. Indeed, some plasticity occurs, but it plays a minor role in hydrogen diffusion.

The position of the concentration peak also advances ahead of the crack tip with a clear monotonic exponential trend as a function of Δa, though it exhibits a stepped pattern due to the numerical discretization and the model's mesh size. Fig. 10.d shows that the peak position is always further from the crack tip at the lower speed, supporting the earlier observations regarding the increased risk of embrittlement. In summary, the plots of Fig. 10.c and d should be considered as tools to describe the concentration field ahead of the crack tip.

5. Discussion

All the input parameters used in the simulations are supported by the experimental characterization campaign performed on the 2.25Cr1Mo steel. These tailored inputs allow for a precise and straightforward outcome of the simulations. Therefore, the damage failure mechanism and the embrittlement effect resulting from hydrogen diffusion at the crack tip are simulated in the most comprehensive manner using cohesive zone models. This choice resulted in some drawbacks for the cohesive elements, especially the N_T-ε_p of Eq. (3) which forces the finite elements to react to plasticity immediately. Indeed, this law differs from other smoother ones presented in the literature (Fig. 2) and suggests that a very small amount of plasticity induces immediate saturation of the dislocation traps. Since they play a meaningful role at the crack initiation, the cohesive elements are somehow unstable, as shown in the initial part of the C_T trend of Fig. 9.a and b. It is worth mentioning that no stabilization is used in the analyses. The use of ABAQUS hourglass control on these trends did not drastically modify the outcomes; moreover, the C_T results also did not vary with a mesh size of 15 μm (half the one for the presented results), which is around the grain size.

Fig. 11 provides additional insights into the relationship between C_L, C_T and ε_p. At the beginning of the analysis, when the material is unstrained, Fig. 11.a shows that the C_{L0}/C_{T0} ratio is 15.0 %. At this ratio, C_T^{ρ} gives the major contribution to the total hydrogen content in the traps. When C_{L0} exceeds 10 wppm, the carbide C_T^c curve rises significantly, while the martensitic laths C_T^m concentration remains much lower. Increasing the strain, e.g. at $\varepsilon_p = 0.6$ which is the maximum value obtained from the simulations, Fig. 11.b shows that the C_L/C_T ratio for the same C_{L0} value is 81.5 %. This suggests that C_T is now comparable in magnitude to C_L. Dislocations are the only active traps, with carbides and martensitic laths being 1.5 and 3 orders of magnitude lower, respectively. This configuration occurs at very low plastic strains. Indeed, due to the formulation of Eq. (3) and as shown in Fig. 11.c, for $\varepsilon_p > 0.1$ the C_T^{ρ} value is almost constant at a fixed C_{L0} value, e.g. with a rapid asymptotic trend. This finding aligns with the results of Fig. 9, which suggests that the

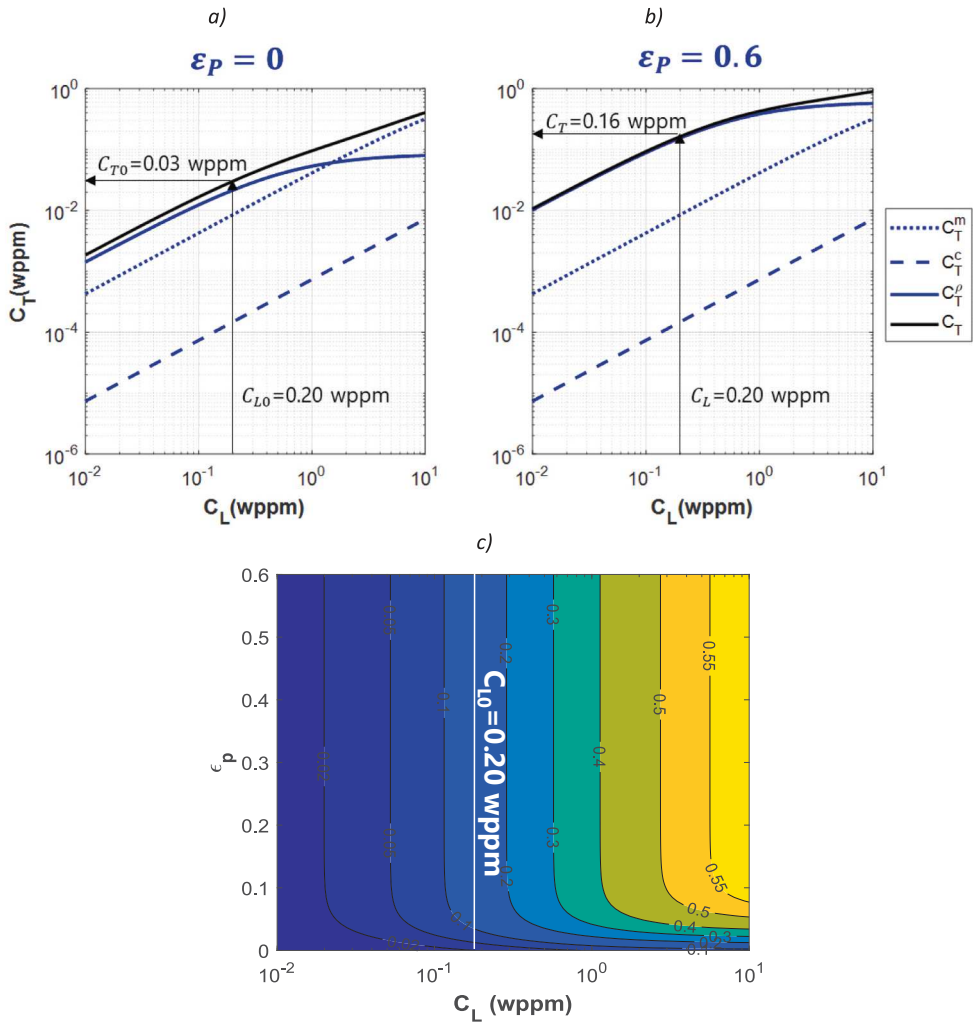

Fig. 11. Plots of hydrogen concentrations C_T in the traps as a function of C_L for a) $\varepsilon_p = 0$, unstrained, and b) $\varepsilon_p = 0.6$. c) C_T levels in wppm as a function of the lattice concentration C_L and the equivalent plastic strain ε_p.

numerical response is initially governed by C_T^o and C_L during crack initiation, where strains are higher. However, in the later propagation stage, the process is mainly driven by the hydrostatic stress gradient field.

6. Conclusions

The work presented a numerical study, supported by experimental inputs, on the 2.25Cr1Mo martensitic steel quenched and tempered at 690 °C. The focus was to simulate the decrease in toughness and embrittlement caused by hydrogen. The key findings of the study can be summarized as follows:

- Experimental fracture surfaces evidenced that the hydrogen embrittlement acting mechanism is HELP mediated HEDE. This mechanism was incorporated into the finite element model of the toughness tests.
- All inputs for the numerical simulations have been collected from experimental tests, including: 1) the stress–strain curve from static tensile tests; 2) the binding energies E_b for each trapping site, e.g. dislocations, martensitic interfaces, and carbides, from thermal desorption analysis; 3) their trap densities N_T from the SEM, the TEM, the TTP curves and the X-ray diffraction; 4) the initial lattice concentration C_{LO} and the diffusion coefficient D_L from the electrochemical permeation experiments.
- The numerical framework was implemented to include a multi-trapping approach. After calibrating the cohesive parameters based on uncharged steel, the model was able to accurately predict the behaviour of hydrogen-charged specimens at different test speeds.
- At the beginning of propagation (0.2 offset line or $CTOD_{0.2}$), dislocation traps assume a primary role and the hydrogen peak is almost coincident with the tip. In this phase, hydrogen embrittlement is quite independent of the test speed, with a critical hydrogen concentration around 2.5 C_{LO}.
- When the propagation proceeds (1.5 offset line or $CTOD_{1.5}$), the critical concentration decreases to the asymptotic value of 1.5 C_{LO}. Besides, hydrogen present in the lattice and other traps generates a peak ahead of the tip, with a difference between the two test speeds. At the lower speed of 1 mm/min, the concentration peak decreases from 2.5 to 2.2 C_{LO} at a maximum distance of 0.15 mm from the actual tip. However, when the test speed decreases to 0.01 mm/min, the peak increases to 2.9•C_{LO} and shifts further to 0.25–0.3 mm ahead of the tip. At the first test speed, the embrittlement is limited, while at the second test speed, the hydrogen effect is evident both from experiments, as suggested by the embrittlement index calculated from the CTOD values and by the fracture surfaces, as well as from the numerical simulations.

In conclusion, the numerical tools provide valuable insights into the concentration fields within the lattice and the various traps that can interact to diffuse hydrogen at the crack tip, at the initiation and during the propagation. In perspective, these numerical models are promising because they are versatile and can predict material behaviour by varying the inputs. For instance, they can be employed for design purposes with metallic materials, to explore their sensitivity to mechanical testing parameters (e.g. different test speeds and initial hydrogen concentrations), material and microstructural properties (e.g. varying trap energies and, consequently, types), as well as chemical parameters (e.g. diffusivity). Moreover, Cohesive Zone Models could be applied not only at the laboratory scale, but also in the design and assessment of industrial components made from metallic materials and exposed to hydrogen, such as vessels and pipelines. This approach is promising despite a few drawbacks, including long computational time and the need to calibrate the Traction Separation Law for mixed-mode loading.

CRediT authorship contribution statement

Chiara Colombo: Writing – review & editing, Writing – original draft, Visualization, Validation, Software, Resources, Methodology, Investigation, Formal analysis, Data curation, Conceptualization. **Luis Borja Peral:** Writing – review & editing, Writing – original draft, Visualization, Validation, Resources, Methodology, Investigation, Formal analysis, Data curation, Conceptualization. **Marcos Bueno:** Data curation, Investigation, Writing – review & editing. **Inés Fernández-Pariente:** Writing – review & editing, Visualization, Supervision, Methodology, Conceptualization.

Declaration of competing interest

The authors declare that they have no known competing financial interests or personal relationships that could have appeared to influence the work reported in this paper.

Acknowledgements

The authors thank Prof Stefano Miccoli from the Department of Mechanical Engineering of Politecnico di Milano for his suggestions on the features implemented in the numerical simulations. Open access funding provided by Politecnico di Milano within the CRUI-CARE Agreement.

Appendix

Table A1
Summary of the experimental tests performed to collect the inputs for the numerical simulations.

Test	Measured quantity	Value	Paper section
Tensile tests (without hydrogen)	*True stress–strain curve, yield stress and ultimate tensile strength*	$\sigma_v = 862 \cdot \varepsilon_{pv}^{0.12} \sigma_{ys} = {}^{430MPa}$ $\sigma_{uts} = 594MPa$	2
Thermal Desorption Analysis	*Diffusible hydrogen content (lattice + reversible traps)*	$C_{L0} + C_{T0} \approx 0.4wppm$	3.1.1
	Trap binding energy for dislocations, Fe_3C carbides, martensitic interfaces	$E_b^o = 29.85\ kJ/mol$ $E_b^m = 20.25\ kJ/mol$ $E_b^c = 14.05\ kJ/mol$	3.1.1, Table 2
X-ray diffraction	*Trap density law for dislocations (from fitting of the experimental data)*	$N_T^o = 10^{24.459 - 0.857exp(-50 \bullet \epsilon_p)} sites/m^3$	3.1.2, Eq. (3)
TTP curves	*Size of the carbide and trap density for Fe_3C carbides*	$N_T^c = 1.25 \cdot 10^{24} sites/m^3$	3.1.3, Eq. (4)
SEM/TEM observations	*Grain size and trap density for martensitic interfaces*	$N_T^m = 5.84 \bullet 10^{24} sites/m^3$	3.1.3, Eq. (5)
Electrochemical permeation experiments	*Diffusivity in the lattice*	$D_L = 5.5 \cdot 10^{-10} m^2/s$	3.1.4, Table 5. *a*
	Initial concentration in the lattice	$C_{L0} \approx 0.2wppm$	3.1.4

Data availability

Data will be made available on request.

References

[1] Draghi M. The future of European competitiveness: Part B, In-depth analysis and recommendations 2024:1–83. https://commission.europa.eu/topics/strengthening-european-competitiveness/eu-competitiveness-looking-ahead_en#paragraph_47059 (accessed May 26, 2025).
[2] Djukic MB, Bakic GM, Sijacki Zeravcic V, Sedmak A, Rajicic B. The synergistic action and interplay of hydrogen embrittlement mechanisms in steels and iron: localized plasticity and decohesion. Engng Fract Mech 2019;216:106528. https://doi.org/10.1016/j.engfracmech.2019.106528.
[3] Dwivedi SK, Vishwakarma M. Hydrogen embrittlement in different materials: a review. Int J Hydrogen Energy 2018;43:21603–16. https://doi.org/10.1016/j.ijhydene.2018.09.201.
[4] Gibala R, Kumnick AJ. Hydrogen trapping in iron and steels. In: Gibala R, Hehemann RF, editors. Hydrog. Embrittlement Stress Corros. Crack., Metals Park, Ohio. Estados Unidos: American Society for Metals; 1984. p. 61–77.
[5] Dadfarnia M, Sofronis P, Neeraj T. Hydrogen interaction with multiple traps: can it be used to mitigate embrittlement? Int J Hydrogen Energy 2011;36:10141–8. https://doi.org/10.1016/j.ijhydene.2011.05.027.
[6] Peral LB, Fernández-Pariente I, Colombo C, Rodríguez C, Belzunce J. The positive role of nanometric molybdenum–vanadium carbides in mitigating hydrogen embrittlement in structural steels. Materials (Basel) 2021;14. https://doi.org/10.3390/ma14237269.
[7] Liu P-Y, Zhang B, Niu R, Lu S-L, Huang C, Wang M, et al. Engineering metal-carbide hydrogen traps in steels. Nat Commun 2024;15:724. https://doi.org/10.1038/s41467-024-45017-4.
[8] Gobbi G, Colombo C, Miccoli S, Vergani L. A weakly coupled implementation of hydrogen embrittlement in FE analysis. Finite Elem Anal Des 2018;141. https://doi.org/10.1016/j.finel.2017.11.010.
[9] Gobbi G, Colombo C, Miccoli S, Vergani L. A fully coupled implementation of hydrogen embrittlement in FE analysis. Adv Engng Softw 2019:135. https://doi.org/10.1016/j.advengsoft.2019.04.004.
[10] Martínez-Pañeda E, Golahmar A, Niordson CF. A phase field formulation for hydrogen assisted cracking. Comput Methods Appl Mech Engng 2018;342:742–61. https://doi.org/10.1016/j.cma.2018.07.021.
[11] Díaz A, Alegre JM, Cuesta II, Martínez-Pañeda E. A COMSOL framework for predicting hydrogen embrittlement, Part I: coupled hydrogen transport. Engng Fract Mech 2025:319. https://doi.org/10.1016/j.engfracmech.2025.111007.
[12] Díaz A, Alegre JM, Cuesta II, Martínez-Pañeda E. A COMSOL framework for predicting hydrogen embrittlement, Part II: phase field fracture. Engng Fract Mech 2025:319. https://doi.org/10.1016/j.engfracmech.2025.111008.
[13] Kim D-H, Sim JM, Chang Y-S, Baek UB. Hydrogen gaseous effects on fracture resistance of API-X70 estimated by XFEM. J Mech Sci Technol 2021;35:3829–35. https://doi.org/10.1007/s12206-021-2106-7.
[14] Fernández-Sousa R, Betegón C, Martínez-Pañeda E. Analysis of the influence of microstructural traps on hydrogen assisted fatigue. Acta Mater 2020;199:253–63. https://doi.org/10.1016/j.actamat.2020.08.030.
[15] Díaz A, Zafra A, Martínez-Pañeda E, Alegre JM, Belzunce J, Cuesta II. Simulation of hydrogen permeation through pure iron for trapping and surface phenomena characterisation. Theor Appl Fract Mech 2020;110:102818. https://doi.org/10.1016/j.tafmec.2020.102818.
[16] Park J, Shin G, Kim H-J, Kim K, Yoon SC, Sohn SS, et al. A continuum scale chemo-mechanical model for multi-trap hydrogen transport in deformed polycrystalline metals. Int J Plast 2024;173:103890. https://doi.org/10.1016/j.ijplas.2024.103890.
[17] ASTM International. ASTM A387/387M-17a: standard specification for pressure vessel plates, alloy steel, chromium-molybdenum 2023: 1–6. doi:10.1520/A0387_A0387M-17AR23.
[18] Peral LB, Amghouz Z, Colombo C, Fernández-Pariente I. Evaluation of hydrogen trapping and diffusion in two cold worked CrMo(V) steel grades by means of the electrochemical hydrogen permeation technique. Theor Appl Fract Mech 2020:110. https://doi.org/10.1016/j.tafmec.2020.102771.
[19] Peral LB, Zafra A, Fernández-Pariente I, Rodríguez C, Belzunce J. Effect of internal hydrogen on the tensile properties of different CrMo(V) steel grades: Influence of vanadium addition on hydrogen trapping and diffusion. Int J Hydrogen Energy 2020;45:22054–79. https://doi.org/10.1016/j.ijhydene.2020.05.228.
[20] Choo WY, Lee JY. Thermal analysis of trapped hydrogen in pure iron. Metall Trans A, Phys Metall Mater Sci 1982;13A:135–40. https://doi.org/10.1007/BF02642424.
[21] Gangloff RP, Somerday BP. Gaseous Hydrogen Embrittlement of Materials in Energy Technologies: Mechanisms. Modelling and Future Developments 2012. https://doi.org/10.1533/9780857095374.

[22] Díaz A, Alegre JM, Cuesta II. A review on diffusion modelling in hydrogen related failures of metals. Engng Fail Anal 2016;66:577–95. https://doi.org/10.1016/j.engfailanal.2016.05.019.
[23] Tien J, Thompson AW, Bernstein IM, Richards RJ. Hydrogen transport by dislocations. Metall Trans A 1976;7:821–9. https://doi.org/10.1007/BF02644079.
[24] Kumnick AJ, Johnson HH. Deep trapping states for hydrogen in deformed iron. Acta Metall 1980;28:33–9. https://doi.org/10.1016/0001-6160(80)90038-3.
[25] Krom AHM, Koers RWJ, Bakker A. Hydrogen transport near a blunting crack tip. J Mech Phys Solids 1999;47:971–92. https://doi.org/10.1016/S0022-5096(98)00064-7.
[26] Huang H, Shaw WJD. Hydrogen embrittlement interactions in cold-worked steel. Corrosion 1995;51:30–6. https://doi.org/10.5006/1.3293573.
[27] Sofronis P, Liang Y, Aravas N. Hydrogen induced shear localization of the plastic flow in metals and alloys. Eur J Mech A/Solids 2001;20:857–72. https://doi.org/10.1016/S0997-7538(01)01179-2.
[28] Falkenberg R. Simulation von Wasserstofftransport und Rißwachstum infolge wasserstoffinduzierter Spannungsrißkorrosion mit einer Analyse der Kopplungsph ¨anomenologie (in German). Kiel: Christian-Albrechts-Universitat; 2010.
[29] Colombo C, Zafra García A, Belzunce J, Fernandez PI. Sensitivity to hydrogen embrittlement of AISI 4140 steel: a numerical study on fracture toughness. Theor Appl Fract Mech 2020:110. https://doi.org/10.1016/j.tafmec.2020.102810.
[30] Thomas RLS, Scully JR, Gangloff RP. Internal hydrogen embrittlement of ultrahigh-strength AERMET 100 steel. Metall Mater Trans A 2003;34:327–44. https://doi.org/10.1007/s11661-003-0334-3.
[31] Zafra A, Belzunce J, Rodríguez C. Hydrogen diffusion and trapping in 42CrMo4 quenched and tempered steel: influence of quenching temperature and plastic deformation. Mater Chem Phys 2020:123599. https://doi.org/10.1016/j.matchemphys.2020.123599.
[32] Peral LB, Fernández-Pariente I, Colombo C. Critical hydrogen concentration for crack propagation in a CrMo steel: targeted experiments for accurate numerical modelling. Engng Fract Mech 2022:273. https://doi.org/10.1016/j.engfracmech.2022.108764.
[33] Nagao A, Dadfarnia M, Somerday BP, Sofronis P, Ritchie RO. Hydrogen-enhanced-plasticity mediated decohesion for hydrogen-induced intergranular and "quasi-cleavage" fracture of lath martensitic steels. J Mech Phys Solids 2018;112:403–30. https://doi.org/10.1016/j.jmps.2017.12.016.
[34] Galindo-Nava EI, Basha BIY, Rivera-Díaz-del-Castillo PEJ. Hydrogen transport in metals: Integration of permeation, thermal desorption and degassing. J Mater Sci Technol 2017;33:1433–47. https://doi.org/10.1016/j.jmst.2017.09.011.
[35] Sofronis P, McMeeking RM. Numerical analysis of hydrogen transport near a blunting crack tip. J Mech Phys Solids 1989;37:317–50. https://doi.org/10.1016/0022-5096(89)90002-1.
[36] Peral LB, Zafra A, Belzunce J, Rodríguez C. Effects of hydrogen on the fracture toughness of CrMo and CrMoV steels quenched and tempered at different temperatures. Int J Hydrogen Energy 2019;44:3953–65. https://doi.org/10.1016/j.ijhydene.2018.12.084.
[37] Novak P, Yuan R, Somerday BP, Sofronis P, Ritchie RO. A statistical, physical-based, micro-mechanical model of hydrogen-induced intergranular fracture in steel. J Mech Phys Solids 2010;58:206–26.
[38] Nagao A, Smith CD, Dadfarnia M, Sofronis P, Robertson IM. The role of hydrogen in hydrogen embrittlement fracture of lath martensitic steel. Acta Mater 2012;60:5182–9. https://doi.org/10.1016/j.actamat.2012.06.040.
[39] Oriani RA. The diffusion and trapping of hydrogen in steel. Acta Metall 1970;18:147–57. https://doi.org/10.1016/0001-6160(70)90078-7.
[40] Gobbi G, Colombo C, Miccoli S, Vergani L. PoliHydra/hydra: fully coupled implementation 2018. doi:10.5281/zenodo.1478086.
[41] Gobbi G, Colombo C, Vergani L. Sensitivity analysis of a 2D cohesive model for hydrogen embrittlement of AISI 4130. Engng Fract Mech 2016;167. https://doi.org/10.1016/j.engfracmech.2016.03.045.
[42] Zafra A, Peral LB, Belzunce J, Rodríguez C. Effects of hydrogen on the fracture toughness of 42CrMo4 steel quenched and tempered at different temperatures. Int J Press Vessel Pip 2019;171:34–50. https://doi.org/10.1016/j.ijpvp.2019.01.020.
[43] Park K, Paulino GH. Cohesive zone models: a critical review of traction-separation relationships across fracture surfaces. Appl Mech Rev 2011:64. https://doi.org/10.1115/1.4023110.
[44] Schwalbe K-H, Scheider I, Cornec A. In: Guidelines for applying cohesive models to the damage behaviour of engineering materials and structures. Berlin Heidelberg: Springer-Verlag; 2013. https://doi.org/10.1007/978-3-642-29494-5.
[45] Tvergaard V, Hutchinson JW. The influence of plasticity on mixed mode interface toughness. J Mech Phys Solids 1993;41:1119–35. https://doi.org/10.1016/0022-5096(93)90057-M.
[46] Hondros ED, Seah MP. Theory of Grain Boundary Segregation in Terms of Surface Adsorption Analogues. Met Trans A 1977;8:A:1363-71. https://doi.org/10.1007/BF02642850.
[47] Serebrinsky S, Carter EA, Ortiz M. A quantum-mechanically informed continuum model of hydrogen embrittlement. J Mech Phys Solids 2004;52:2403–30. https://doi.org/10.1016/j.jmps.2004.02.010.
[48] Jiang DE, Carter EA. First principles assessment of ideal fracture energies of materials with mobile impurities: Implications for hydrogen embrittlement of metals. Acta Mater 2004;52:4801–7. https://doi.org/10.1016/j.actamat.2004.06.037.
[49] Fréchet MM. Sur quelques points du calcul fonctionnel. Rend Del Circ Mat Di Palermo 1906;22:1–72. https://doi.org/10.1007/BF03018603.
[50] Alvaro A, Olden V, Akselsen OM. 3D cohesive modelling of hydrogen embrittlement in the heat affected zone of an X70 pipeline steel. Int J Hydrogen Energy 2013;38:7539–49. https://doi.org/10.1016/j.ijhydene.2013.02.146.
[51] Suman S, Khan MK, Pathak M, Singh RN. 3D simulation of hydride-assisted crack propagation in zircaloy-4 using XFEM. Int J Hydrogen Energy 2017;42:18668–73. https://doi.org/10.1016/j.ijhydene.2017.04.163.
[52] Kristensen PK, Niordson CF, Martínez-Pañeda E. Applications of phase field fracture in modelling hydrogen assisted failures. Theor Appl Fract Mech 2020:110. https://doi.org/10.1016/j.tafmec.2020.102837.